

ARTICLE

Received 19 Jun 2015 | Accepted 10 Feb 2016 | Published 17 Mar 2016

DOI: 10.1038/ncomms11009

OPEN

Design and synthesis of the superionic conductor $\text{Na}_{10}\text{SnP}_2\text{S}_{12}$

William D. Richards¹, Tomoyuki Tsujimura², Lincoln J. Miara³, Yan Wang¹, Jae Chul Kim^{1,4}, Shyue Ping Ong⁵, Ichiro Uechi², Naoki Suzuki² & Gerbrand Ceder^{1,4,6}

Sodium-ion batteries are emerging as candidates for large-scale energy storage due to their low cost and the wide variety of cathode materials available. As battery size and adoption in critical applications increases, safety concerns are resurfacing due to the inherent flammability of organic electrolytes currently in use in both lithium and sodium battery chemistries. Development of solid-state batteries with ionic electrolytes eliminates this concern, while also allowing novel device architectures and potentially improving cycle life. Here we report the computation-assisted discovery and synthesis of a high-performance solid-state electrolyte material: $\text{Na}_{10}\text{SnP}_2\text{S}_{12}$, with room temperature ionic conductivity of 0.4 mS cm^{-1} rivalling the conductivity of the best sodium sulfide solid electrolytes to date. We also computationally investigate the variants of this compound where tin is substituted by germanium or silicon and find that the latter may achieve even higher conductivity.

¹ Department of Materials Science and Engineering, Massachusetts Institute of Technology, Cambridge, Massachusetts 02139, USA. ² Samsung R&D Institute Japan, Minoh Semba Center Building 13F, Semba Nishi 2-1-11, Minoh, Osaka 562-0036, Japan. ³ Samsung Advanced Institute of Technology—USA, 255 Main Street, Suite 702, Cambridge, Massachusetts 02142, USA. ⁴ Materials Sciences Division, Lawrence Berkeley National Laboratory, Berkeley, California 94720, USA. ⁵ Department of NanoEngineering, University of California San Diego, La Jolla, California 92093-0448, USA. ⁶ Department of Materials Science and Engineering, University of California Berkeley, Berkeley, California 94720, USA. Correspondence and requests for materials should be addressed to G.C. (email: gceder@berkeley.edu).

The energy density and cycle life of intercalation batteries has made them the dominant technology in all manner of applications, from consumer electronics to electric vehicles and high-performance batteries in commercial aircraft. A potential key application of sodium (Na)-ion battery technology is grid-scale energy storage due to its lower cost relative to lithium (Li)-ion. In addition to sodium being considerably more abundant than Li, Na-ion batteries have the advantage of a broader range of available cathode materials since many layered Li-transition metal oxides show improved performance in their sodium versions^{1–3}. In addition, many high capacity Na-cathodes do not contain cobalt, an expensive and scarce component of many commercial Li-ion cathodes. The choice of electrolyte for Na-ion systems is not as well established as for Li-ion, but the vast majority of electrolytes in development are based on organic solvents⁴. These suffer from the same flammability concerns as their counterparts in lithium batteries, and are exacerbated by the presence of a much more reactive metal. In addition, heat dissipation properties of the battery are worsened by the size of installations required for grid storage, and thermal runaway is therefore an even greater concern than at smaller scales. The creation of low-temperature sodium-solid electrolytes would go a long way towards the development of safe solid-state Na-ion batteries, free of flammable solvents.

Despite much work in the area, no anode materials for sodium ion systems have been found that can match the conductivity, energy density and price of graphite anodes in Li-ion batteries. Though hard carbon anodes have been shown to reversibly intercalate sodium⁵, capacity is very low compared with that allowed by intercalation to LiC₆ (ref. 6). Solid electrolytes may also suppress dendrite formation, enabling the use of sodium metal anodes and improving battery capacity considerably.

Na-solid electrolytes have been commercialized in high-temperature batteries such as β -alumina for sodium-sulfur (NAS) batteries⁷, yet few materials with high conductivities at low temperature have been reported. Conductivities over 1 mS cm⁻¹ have been shown in NASICON-type oxide crystals^{8,9}, but processing of these materials at high temperatures (typically >1,000 °C (refs 7,10)) is required to reduce grain boundary resistance, which is incompatible with typical cathode materials and complicates battery fabrication. In both sodium and lithium systems, thiophosphate materials are promising candidates as solid electrolytes as they are soft and can be incorporated into batteries by cold pressing without requiring high-temperature sintering. In 2011, Kamaya *et al.* reported the synthesis of Li₁₀GeP₂S₁₂ (LGPS), a tetragonal structure within the Li_{3+x}Ge_xP_{1-x}S₄ thiophosphate system that achieves 12 mS cm⁻¹ conductivity at room temperature¹¹, and in 2014 Seino *et al.* reported a conductivity of 27 mS cm⁻¹ with a glass-ceramic electrolyte composed of Li₇P₃S₁₁ crystals precipitated from a glass¹². There has been relatively less experimental work done on sodium systems, though recently the cubic phase of Na₃PS₄ has been reported to have conductivity as high as 0.46 mS cm⁻¹, and has been used in an all-solid-state battery^{13,14}. Similar to lithium materials, Si doping has recently been used to increase defect concentrations in Na₃PS₄, resulting in a conductivity of 0.7 mS cm⁻¹ (ref. 15). For construction of solid-state cells, low-strain electrodes^{16,17} are also important to minimize delamination of the electrolyte, especially when using harder electrolyte materials such as oxides.

Ab initio calculation of material properties can rapidly speed up the search for new solid electrolyte materials, allowing prediction of as-yet-undiscovered materials through calculations of phase diagrams¹⁸ and evaluation of the diffusivity of carefully controlled structures, which normally can only be achieved experimentally after a long process of synthesis optimization. Even when new hypothetical materials show similarity to existing

materials, chemical intuition alone cannot reliably determine which chemical modifications will result in experimentally realizable structures, for example, the high conductivity lithium garnets¹⁹ have no direct sodium analogues. *Ab initio* calculations have shown remarkable accuracy in predicting the properties of Li-solid-state conductors^{11,20–24}. Here we present computational predictions of three Na-ion conductors crystallizing in the high-conductivity tetragonal structure and with conductivities equalling and exceeding the current best performing materials. We also show experimental results confirming our prediction of the Na₁₀SnP₂S₁₂ material, with experimentally measured conductivity and activation energy in excellent agreement with the *ab initio* result. In addition to rigorously probing the energetics and hence feasibility of synthesis of these materials, computational techniques are able to give an indication of their performance. They are thus able to focus experimental efforts on systems with a high probability of success. These results highlight the predictive nature of first principles calculations—in addition to explaining difficult to observe phenomena, they can be used to discover compounds with extraordinary physical properties.

Results

General considerations. Using first principles computation, we evaluate three key properties of the tetragonal phases of Na₁₀MP₂S₁₂ (M = Si, Ge, Sn) to determine their suitability as a solid-state electrolyte materials: (1) we determine the Na⁺ conductivity and its activation energy from *ab initio* molecular dynamics (AIMD) simulations, (2) using high-throughput computations and structure prediction methods, we comprehensively calculate the ground-state phase diagram of each system to gauge the stability and synthesizability of each compound and (3) we extract the electrochemical anodic and cathodic stability limits from the grand canonical equilibrium at various potentials similar to the approach described in an earlier work²⁵. Based on this data, we then proceeded to synthesize and test Na₁₀SnP₂S₁₂.

Ground-state energy calculations. Since there is typically considerable cation site disorder in these conductors, we used an electrostatic energy criterion to pre-screen Na/Vacancy orderings on the experimentally reported structure of LGPS²⁶. For each of the three symmetrically distinct M/P orderings and for full and half Na4 site occupancy, we relaxed the structures of the lowest electrostatic energy arrangements using density functional theory (DFT), taking the lowest energy of these as the 0 K enthalpy and structure. The structure of Na₁₀MP₂S₁₂ (NMPS) can be described as consisting of three symmetrically distinct chains of cations oriented parallel to the *c*-axis (Fig. 1). At unit cell coordinates $x = 0.25, y = 0.25$, tetrahedral Na sites (Na1, Na3) form a chain of partially occupied edge-sharing sites. At $x = 0, y = 0.5$ there is an edge-sharing chain of alternating Na_{oct} and (M/P)_{tet} sites. At $x = 0, y = 0$, a similar chain but with a vacancy instead of M cation and more distorted Na_{oct} site is present (with repeat unit Na_{oct}-P_{tet}-Na_{oct}-Vac_{tet}). The *ab initio* MD results will demonstrate that the (Na1, Na3) chains carry most of the Na conductivity with occasional crossover through the Na sites in the chain at $x = 0, y = 0$. The ground state M/P ordering, which is found to be shared among all studied chemistries, is shown in Fig. 1 and the ground-state Na-ion arrangement (C222 space group) in Supplementary Fig. 2.

***Ab initio* molecular dynamics.** The Na-ionic conductivity (σ), and activation energy (E_a) were determined from AIMD simulations between 600 and 1,300 K and extrapolated to room

temperature. Ionic conductivity is calculated from AIMD through the intermediate calculation of D_σ , which has the units of a diffusivity but takes into account correlations between Na-ions (see Methods). The results are shown in Fig. 2a, and compared with similar Li compounds in Table 1. The self diffusivity (D_{self}) of the Na-ions was also calculated for comparison, with results included in Supplementary Table 1 and Supplementary Fig. 1. For both the Li and Na materials, activation energy slightly increases as M changes from Si \rightarrow Ge \rightarrow Sn. Somewhat surprisingly, given the size difference between Na and Li ions, Na and Li materials have similar activation energies, resulting in high room temperature conductivities particularly for the Ge and Si materials, which are predicted to have room temperature conductivities comparable to those of organic electrolytes⁴. Our result for $\text{Na}_{10}\text{GeP}_2\text{S}_{12}$ is similar to the result of ref. 27. These conductivities are more impressive, given that they are entirely due to Na^+ motion, and so the transference number is equal to 1. The degree of cooperativity of ionic motion is described by the Haven ratio H_r (ref. 28), which we calculate from the ratio of D_{self} to D_σ . This value is calculated to be ~ 0.56 in all of our simulations, which is slightly smaller than that observed experimentally for the lithium versions of these materials^{22,23}, indicating a larger degree of cooperative motion.

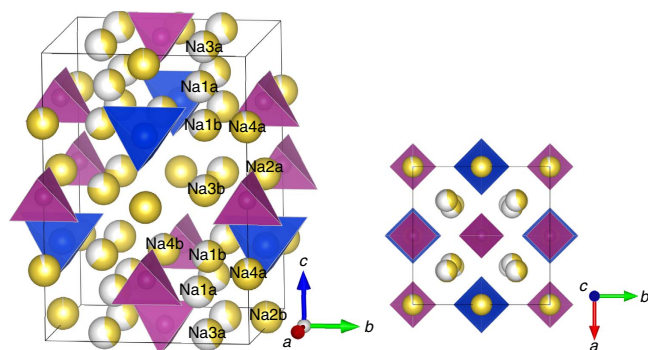


Figure 1 | Structure of $\text{Na}_{10}\text{SnP}_2\text{S}_{12}$ from DFT calculations. Sodium occupancies are calculated from 600 K AIMD simulation (see Methods). All ground-state NMPS structures share this M/P ordering, which reduces the symmetry from the $P4_2/nmc$ space group to $P\bar{4}m2$, separating each Na-site into two symmetrically distinct but similar sites marked as *a* and *b*. PS_4 tetrahedra are marked in purple, SnS_4 tetrahedra in blue and Na-sites in yellow. The ground-state Na-ordering is shown in Supplementary Fig. 2.

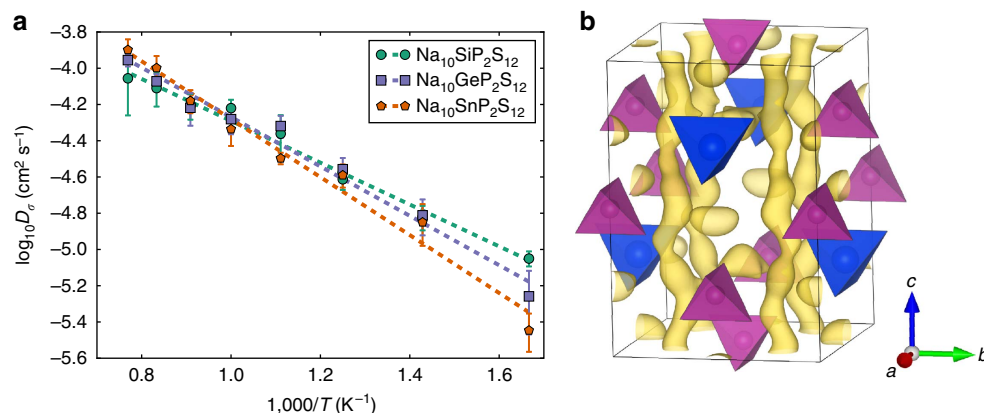


Figure 2 | DFT computed diffusivity of $\text{Na}_{10}\text{SnP}_2\text{S}_{12}$. (a) Na-diffusivity in $\text{Na}_{10}\text{SiP}_2\text{S}_{12}$, $\text{Na}_{10}\text{GeP}_2\text{S}_{12}$ and $\text{Na}_{10}\text{SnP}_2\text{S}_{12}$ from AIMD simulation. Dashed lines are Arrhenius fits to the data, and error bars are standard error of the mean. (b) Na-ion probability density isosurface (yellow) of $\text{Na}_{10}\text{SnP}_2\text{S}_{12}$ from 600 K AIMD simulation. SnS_4 tetrahedra are marked in blue, PS_4 tetrahedra in purple.

Phase diagrams and stability limits. To determine the feasibility of synthesizing these high conductivity tetragonal phases of $\text{Na}_{10}\text{MP}_2\text{S}_{12}$ ($M = \text{Si}, \text{Ge}, \text{Sn}$), we used DFT to evaluate the energies of materials and generate their respective quaternary phase diagrams. To obtain appropriate competing phases in the quaternary phase diagrams, we calculated the energy of a very large number of compounds in their relevant chemical spaces, including all known materials present in the Inorganic Crystal Structure Database (ICSD)²⁹ containing some or all of the four elements, all relevant materials derived from substituting sodium for lithium in all ICSD materials and the $\text{Li}_x\text{P}_y\text{S}_z$ structures compiled by Lepley *et al.*³⁰. To further improve the coverage of these chemical spaces, we also applied the data-mined substitution methodology of Hautier *et al.*¹⁸ to predict possible structures from a broader range of chemistries in the ICSD. The 0 K phase diagram for Na-Sn-P-S is shown in Fig. 3. Na-Ge-P-S and Na-Si-P-S phase diagrams are available in Supplementary Fig. 3.

No quaternary ground states are found in any of the three systems. Decomposition energy (E_{decomp}) to the equilibrium ground-state structures is calculated using the convex hull method implemented in pymatgen³¹ and is shown in Table 2, and compared with their lithium counterparts. For example, the stability of the $\text{Na}_{10}\text{SnP}_2\text{S}_{12}$ phase is given by the calculated enthalpy of the decomposition reaction $\text{Na}_{10}\text{SnP}_2\text{S}_{12} \rightarrow 2 \text{Na}_3\text{PS}_4 + \text{Na}_4\text{SnS}_4$. Even though all the considered electrolyte structures show a small driving force at 0 K to decompose to $(\text{Li}/\text{Na})_4\text{MS}_4$ ($M = \text{Si}, \text{Ge}, \text{Sn}$) and $(\text{Li}/\text{Na})_3\text{PS}_4$, this is similar to the Li-analogues that have similar decomposition energies, and have all been synthesized^{11,21,23,24}. We expect high configurational entropy on the cation sites to result in their stabilization at moderate temperatures. An approximation of this entropy, neglecting the ion-ion interactions, can be obtained using the formula $S = -k_B \sum_i p_i \ln p_i$, where k_B is the Boltzmann constant, p_i is the probability of each state (occupied or unoccupied) and the sum is over all states for each site. Using a value of 50% occupancy of the Na-atoms in the edge-sharing *c*-axis chains and 50% M/P occupancy (28 sites with 50% occupancy per 50 atom unit cell) yields a value of $0.0334 \text{ meV K}^{-1}$ per atom, which at 300 K already would stabilize the Sn and Ge compositions. This is an upper bound on the configurational entropy but vibrational entropy, particularly the soft phonon modes of the diffusing ions, is also expected to contribute to the structure's stabilization. Table 2 also shows the calculated anodic and cathodic stability limits evaluated from the chemical potentials of Na at which the compound decomposes, following the methods of ref. 25. Since

Table 1 | Ionic conductivity of cation-substituted compounds $X_{10}MP_2S_{12}$.

Compound	DFT simulation		Experimental	
	E_a (eV)	Conductivity, 298 K (mS cm^{-1})	E_a (eV)	Conductivity, 298 K (mS cm^{-1})
$\text{Na}_{10}\text{SiP}_2\text{S}_{12}$	0.229	10.28	NA	NA
$\text{Na}_{10}\text{GeP}_2\text{S}_{12}$	0.270	3.50	NA	NA
$\text{Na}_{10}\text{SnP}_2\text{S}_{12}$	0.317	0.94	0.356	0.4 (this work)
$\text{Li}_{10}\text{SiP}_2\text{S}_{12}$	0.20	23 (ref. 20)	0.196	2.3 (ref. 21)
$\text{Li}_{10}\text{GeP}_2\text{S}_{12}$	0.21	13 (ref. 20)	0.22–0.25	9–12 (refs 11,22)
$\text{Li}_{10}\text{SnP}_2\text{S}_{12}$	0.24	6 (ref. 20)	0.24–0.27	4–7 (refs 23,24)

NA, not applicable. DFT simulation and experimental results on the sodium structures are from this work. Experimental and calculated values for the Li compounds are taken from the literature.

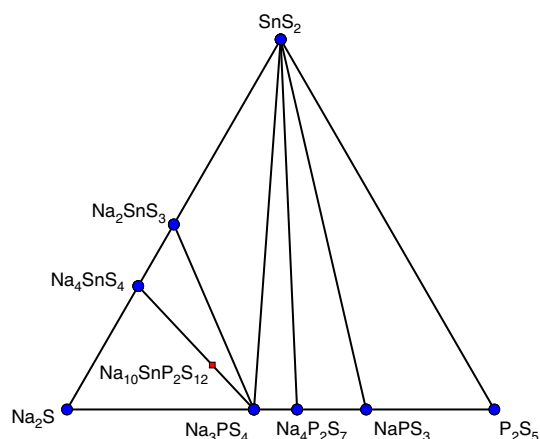


Figure 3 | Na-Sn-P-S phase diagram. Pseudo-ternary 0 K Na-Sn-P-S phase diagram constructed from DFT energy calculations, with location of $\text{Na}_{10}\text{SnP}_2\text{S}_{12}$. Stable phases marked with blue dot.

these materials by our calculations are metastable at 0 K, we instead consider the potentials at which the ground-state materials equilibrium becomes unstable, for example, for $\text{Na}_{10}\text{SnP}_2\text{S}_{12}$, when either Na_4SnS_4 or Na_3PS_4 becomes unstable.

When the chemical potential (voltage) of the alkali is below (above) the stable region (as can be experienced at the cathode interface during charging), the ion and its associated electron is pulled from the electrolyte, which decomposes into a mixture of sulfides and elemental sulfur (for example, Na_4SnS_4 decomposes to S and Na_2SnS_3 above 1.82 V versus Na metal, and S and SnS_2 above 2 V). In contact with the anode (cathodic limit), the Li/Na metal may reduce the metal or phosphorus in the electrolyte, potentially leading to electron conductivity through the electrolyte if this reaction continues without passivation. The cathodic limit for Na and Li compounds is set by the partial reduction of phosphorus to form Na_2PS_3 , and the calculated cathodic stability is thus unaffected by the choice of metal (M) cation. The potentials at which the metal cation is fully reduced by the alkali are also listed in Table 2, and indicate the potential at which the decomposition reaction is no longer passivating. The shift in the stability window between the Na and Li materials is due to the differing reduction potentials of the alkali metal. Previous DFT studies have shown that this reduction reaction can be passivated in some systems by the formation of a thin layer of Li_2S (ref. 30), though in practice insulating barrier coatings are typically employed at the anode/cathode interfaces^{11,32,33}. The anodic voltage stability limit is set primarily by the reaction energy of the alkali metal with elemental sulfur, though in compounds with highly negative enthalpies of mixing from the binary sulfides the stability range is extended slightly. This effect is small in the considered electrolyte materials,

with the anodic stability only changing on the order of 0.1 V between materials with different (M) cations.

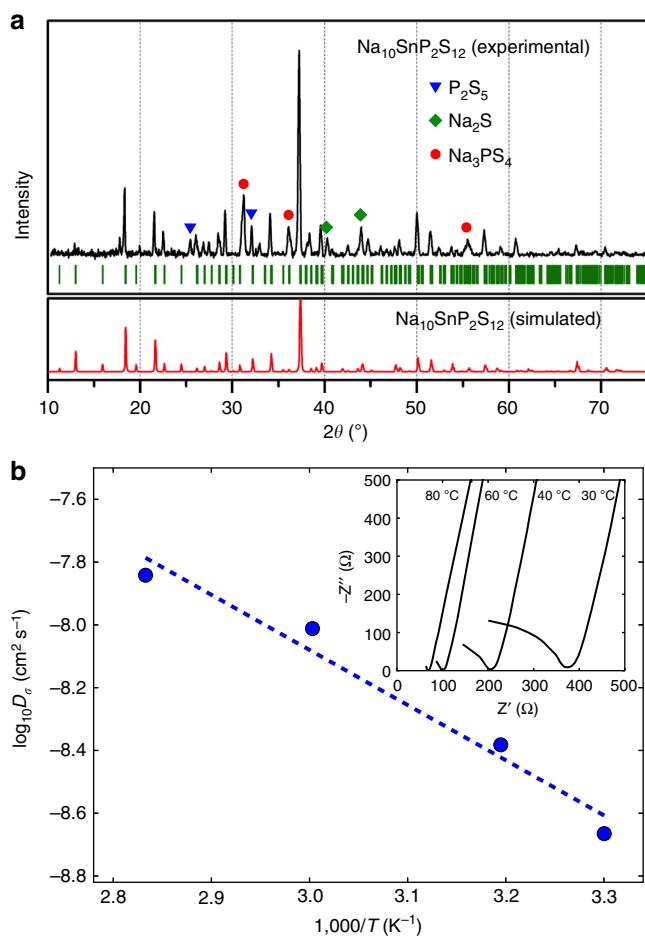
Synthesis and experimental verification. In validation of our computational predictions, we report successful synthesis of $\text{Na}_{10}\text{SnP}_2\text{S}_{12}$, which was chosen due to its low materials cost and E_{decomp} of 7.1 meV per atom, which is lower than comparable materials that have been synthesized. $\text{Na}_{10}\text{SnP}_2\text{S}_{12}$ was prepared from the binary sulfide phases (see Methods), under a range of cooling rates. The lattice volume and conductivity of the synthesized phase increase as the cooling rate is lowered (Supplementary Fig. 4), with the highest conductivity achieved by cooling from 700 °C over 99 h. To compare the experimental XRD pattern with that predicted from DFT calculation, we used the Na and Sn/P site disordered structure with positions and fractional occupancies of each site generated from k -means clustering of Na-position data from the 600 K AIMD simulation as a starting point for powder XRD simulation of the structure. Comparison of the simulated and experimental XRD patterns is shown in Fig. 4a. The obtained material is predominantly the expected tetragonal $\text{Na}_{10}\text{SnP}_2\text{S}_{12}$, with small amounts of P_2S_5 , Na_3PS_4 , primarily in the tetragonal α -phase as indicated by the peak splitting at 31 and 36 degrees¹³, and Na_2S , which formed during the slow cooling. At faster cooling rates, these impurity phases do not form but the resulting material has lower conductivity due to the lower lattice volume. The change in the lattice volume and conductivity is likely a result of the structure in the slow cooled sample having a higher ratio of Sn to P, since the observed impurities contain no Sn. Similar dependency of conductivity and lattice volume on this ratio are seen in the lithium systems³⁴. The low conductivity of the impurity phases the slow-cooled sample are expected to reduce the measured conductivity by reduction in the effective cross-sectional area. The strong relation between lattice volume and conductivity also support the conductivity measured in the slow-cooled sample being that of $\text{Na}_{10}\text{SnP}_2\text{S}_{12}$.

The intensities of the 011 and (110 and 002) reflections, producing XRD peaks at 12 and 16 degrees, vary as a function with cooling rate, but are not strongly correlated with conductivity. Supplementary Fig. 5 shows the XRD spectrum of a quenched sample in which these low-angle peaks are more clearly visible. The variation in these peak intensities may be caused either by slight disorder between the P_{tet} , M_{tet} and Vac_{tet} sites, or by changes in average size of the $(\text{Sn}/\text{P})\text{S}_4$ tetrahedra from slight compositional variation.

Considering that AIMD simulations were performed at elevated temperatures and extrapolated to experimental conditions, the conductivity predicted from these simulations is in remarkable agreement to our experimental electrochemical impedance spectroscopy results (Fig. 4b). We predicted a room temperature conductivity of 0.94 mS cm^{-1} with activation energy

Table 2 | Phase equilibria decomposition enthalpies and stability ranges for $X_{10}MP_2S_{12}$.

Cation(X)	Cation(M)	Decomposition products	E_{decomp} (meV per atom)	Metal reduction (V versus metal anode)	Cathodic stability (V versus metal anode)	Anodic stability (V versus metal anode)
Na	Si	$\text{Na}_4\text{SiS}_4 + 2 \text{Na}_3\text{PS}_4$	13.6	0.80	1.25	1.77
	Ge	$\text{Na}_4\text{GeS}_4 + 2 \text{Na}_3\text{PS}_4$	7.2	1.10	1.25	1.70
	Sn	$\text{Na}_4\text{SnS}_4 + 2 \text{Na}_3\text{PS}_4$	7.1	1.09	1.25	1.82
Li	Si	$\text{Li}_4\text{SiS}_4 + 2 \text{Li}_3\text{PS}_4$	14.9	1.36	1.78	2.14
	Ge	$\text{Li}_4\text{GeS}_4 + 2 \text{Li}_3\text{PS}_4$	14.7	1.64	1.78	2.06
	Sn	$\text{Li}_4\text{SnS}_4 + 2 \text{Li}_3\text{PS}_4$	13.4	1.57	1.78	2.02

**Figure 4 | Experimental crystal structure and diffusivity of $\text{Na}_{10}\text{SnP}_2\text{S}_{12}$.**

(a) Experimental and simulated XRD patterns of $\text{Na}_{10}\text{SnP}_2\text{S}_{12}$, showing small amounts of recrystallized P_2S_5 , Na_3PS_4 and Na_2S . (b) Diffusivity calculated from experimentally measured ionic conductivity versus temperature. Dashed line is an Arrhenius fit to the data. (inset) Electrochemical impedance spectroscopy measurements.

of 317 meV, while experimentally $\text{Na}_{10}\text{SnP}_2\text{S}_{12}$ shows a conductivity of 0.4 mS cm^{-1} with an activation energy of 356 meV.

Discussion

$\text{Na}_{10}\text{SnP}_2\text{S}_{12}$ is a remarkably good ionic conductor; its room temperature conductivity of 0.4 mS cm^{-1} is comparable to the

best performing sulfide electrolyte to date—cubic Na_3PS_4 , which achieves conductivities of between 0.2 and 0.7 mS cm^{-1} depending on doping and processing conditions^{13–15}. These thiophosphate electrolytes benefit from improved processability relative to the oxide β -alumina and NASICON-based compounds, which can have higher conductivities but require high-temperature sintering, making them difficult to incorporate into room temperature batteries. To evaluate the potential for even better conductors in this family of compounds, we investigate in more detail the conductivity mechanism in these compounds and the effect of the main group metal (Si, Ge, Sn) on it.

From our DFT calculations, we see that the activation energy for Na diffusion in the NMPS materials shown in Fig. 2a increases as the ionic radius of the (M)etal in the compound increases, with $E_a^{\text{Si}} < E_a^{\text{Ge}} < E_a^{\text{Sn}}$. This trend is also seen in activation energies for the Li conductors, both in experimental and DFT studies (Table 1). This is surprising since often the activation energy barrier between adjacent sites in a structure decreases as the size of the anion framework increases. In the NMPS conductors, however, the lattice parameter differences are small ($< 1\%$, Supplementary Table 2), and the activation energy actually increases as the cell volume increases. The valence of the other cations near the transition state has been pointed to as an important factor as it can increase the activation energy by strong repulsion of the alkali in the activated state^{35,36}, but this is unlikely to play a role here as Si, Ge and Sn all have valence $4+$. Hence, because of their similar volume and cation valence, these three compounds form a good data set to evaluate potentially more subtle chemical influences on the conductivity. To understand the somewhat counterintuitive result, we examine the diffusion paths and site occupancies in each compound as a measure of the free-energy landscape of the structures.

From the AIMD Na-ion trajectories, we calculate the Na-ion probability density, defined as the time-averaged Na-ion occupancy, allowing visualization of the Na-ion diffusion mechanism. The probability density from AIMD simulation of $\text{Na}_{10}\text{SnP}_2\text{S}_{12}$ at 600 K in Fig. 2b is representative of all of our AIMD simulations, and shows that the majority of the Na diffusion occurs within the c -axis chain of partially occupied Na sites at $x = 0.25$ and $y = 0.25$, with some crossover between these channels. These results are in good qualitative agreement with the highly anisotropic Li sites seen in previous spectroscopic studies on LGPS^{11,26}.

The Na-site occupancies of the three materials as a function of simulation temperature are shown in Fig. 5. $P4_2/nmc$ spacegroup operations are applied to the Na-positions before analysis to undo the splitting of Na sites caused by the M/P ordering and shown in

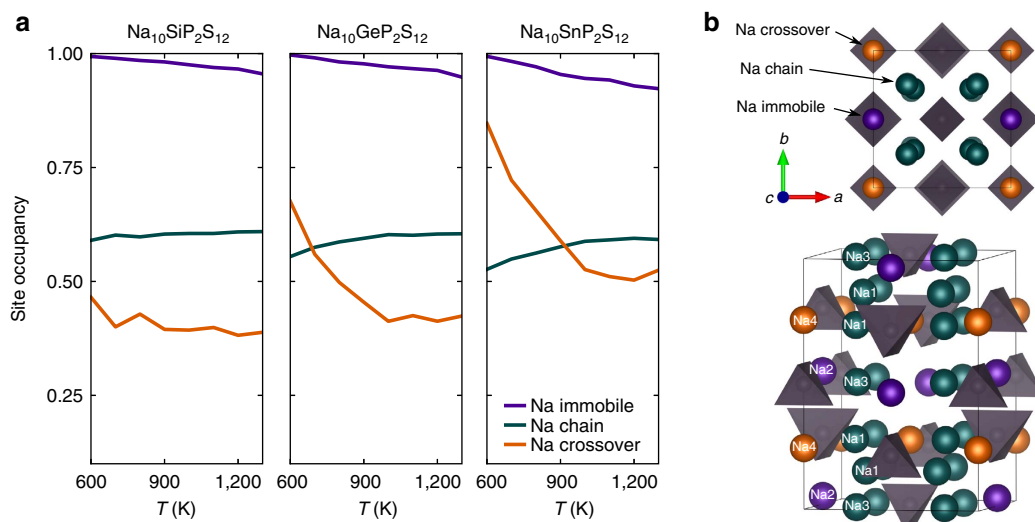


Figure 5 | Na-site occupancy analysis of NMPS structures. (a) Occupancy of Na sites in $\text{Na}_{10}\text{SiP}_2\text{S}_{12}$, $\text{Na}_{10}\text{GeP}_2\text{S}_{12}$ and $\text{Na}_{10}\text{SnP}_2\text{S}_{12}$ from AIMD simulation between 600 and 1,300 K, after imposing PA_2/nmc spacegroup operations. The site occupancies in the Na-chain (Na1 and Na3) have been combined for clarity. (b) Illustration of the Na-chain, Na-crossover and Na-immobile sites. SnS_4 and PS_4 tetrahedra (grey), all spheres are Na-sites.

Fig. 1. Trends in occupancy are similar for Na-sites that are part of the same c -axis cation chain, again confirming a flat energy landscape and high mobility along it. These Na-ion diffusion pathways are connected to each other through the Na4 (Na-crossover) sites, which are part of the $\text{Na}_{\text{oct}}\text{-P}_{\text{tet}}\text{-Na}_{\text{oct}}\text{-Va}_{\text{c,tet}}$ chain along the c -axis at $x=0, y=0$. The Na-sites in the fully occupied $\text{Na}_{\text{oct}}\text{-P}_{\text{tet}}\text{-Na}_{\text{oct}}\text{-M}_{\text{tet}}$ c -axis chain at $x=0, y=0.5$ have low energy and high occupancy, and are labelled as Na-immobile sites in Fig. 5 as they are not expected to contribute strongly to diffusion at low temperatures.

At high temperatures, the occupancies of each Na-site are almost identical across the three chemistries, indicating that they are dominated by entropic effects and not by the specific enthalpic differences between the compounds. At low temperatures, relative occupancies are more dependent on differences in site enthalpy. Considering first the Sn material, the occupancy of the Na-crossover sites dramatically increases as temperature is reduced, indicating that the enthalpy of the Na-crossover sites is significantly lower than the Na-chain sites. In contrast to $\text{Na}_{10}\text{SnP}_2\text{S}_{12}$, occupancy of the Na-crossover sites in the Si material is relatively unaffected by temperature, indicating minimal site enthalpy difference between the Na-chain and Na-crossover sites. The behaviour of occupancies in $\text{Na}_{10}\text{GeP}_2\text{S}_{12}$ is between these two extrema.

The diffusivity of Na-ions is determined primarily by the smoothness of their free-energy landscape. In materials where atoms can be trapped in very low-energy minima, activation energy for moving between these sites is increased, and thus diffusivity is reduced. The trends in Na-crossover site energy correlate well with the activation energies observed in simulation and explain why $\text{Na}_{10}\text{SiP}_2\text{S}_{12}$ has the highest predicted conductivity. At low T , the energy of the Na in the chain and crossover sites are almost equal, allowing Na to migrate in three dimensions with a very low barrier.

The good correspondence between the simulated and experimental results highlight the value of DFT as a predictive tool for the identification of new electrolyte materials. In this work, we focused synthesis efforts on the Sn material due to its affordability relative to the Ge version as well as its low E_{decomp} of 7.1 meV per atom, which is lower than comparable materials that have been synthesized. In LGPS and related lithium electrolytes,

contact with the highly reducing lithium metal or graphite anode can cause electrolyte decomposition by reduction of the transition metal. For these sodium electrolytes this may be less of a concern due to the lower reduction potential of sodium. These newly predicted materials may also prove to be more stable in battery applications than cubic Na_3PS_4 material, since decomposition of $\text{Na}_{10}\text{MP}_2\text{S}_{12}$ requires diffusion of high-valent cations to form Na_3PS_4 and Na_4MS_4 , in contrast to cubic Na_3PS_4 , which can convert to a low conductivity tetragonal phase³⁷ at the same composition. The conductivity of the new $\text{Na}_{10}\text{SnP}_2\text{S}_{12}$ electrolyte rivals that of the best known sulfide sodium-conductors, and the predicted Ge and Si materials, if confirmed, have the potential to surpass the conductivities of all known Na-electrolytes in a system much more compatible with all solid-state battery fabrication than NASICON-based and other oxide electrolytes.

In this work, we used first principles calculation to predict the existence of several new high-performance sodium electrolyte materials, with excellent agreement to subsequent experimental results. This marks the first use of computational prediction to design novel sodium electrolytes. The resulting $\text{Na}_{10}\text{SnP}_2\text{S}_{12}$ electrolyte, with a conductivity of 0.4 mS cm^{-1} at room temperature and activation energy of 0.35 eV, rivals the best known sulfide sodium-electrolytes and our predicted materials have the potential to surpass this conductivity. Our study highlights the benefits that can be gained by using *ab initio* approaches to guide material discovery.

Methods

Density functional theory calculations. All *ab initio* structure calculations were performed with calculations implemented in VASP³⁸, using the projector augmented-wave method³⁹. Calculations used the Perdew–Burke–Ernzerhof generalized-gradient approximation⁴⁰. For energy calculations of NMPS structures, a Monkhorst–Pack k -point grid of $4 \times 4 \times 4$ was used, for other competing phases, k -points were chosen such that $n_{\text{kpoints}} \times n_{\text{atoms}} > 1,000$. The VASP pseudopotential set of Li (PAW_PBE Li 17Jan2003), Na (PAW_PBE Na 08Apr2002), Ge (PAW_PBE Ge 05Jan2001), Si (PAW_PBE Si 05Jan2001), Sn (PAW_PBE Sn_d 06Sep2000), P (PAW_PBE P 17Jan2003) and S (PAW_PBE S 17Jan2003) was used.

Phase diagrams and stability limits. Phase diagrams are constructed using pymatgen³¹ by computing the lower convex hull of DFT computed energy per atom in composition space, similar to the work in ref. 25. Materials on this convex hull cannot decompose to a lower energy combination of phases and are therefore stable. Grand potential phase diagrams are constructed by computing the lower

convex hull of the DFT computed grand potential ($\Phi_{[c,\mu_{\text{Li}}]} = E[c] - n_{\text{Li}}[c]\mu_{\text{Li}}$, where $E[c]$, $n_{\text{Li}}[c]$ and μ_{Li} are the DFT computed energy, lithium content and lithium chemical potential of composition c in composition space. Anodic and cathodic stability limits are given by the maximum and minimum lithium chemical potentials for which a material (or its 0 K decomposition products in the case of metastable structures) is found to be stable.

Conductivity simulations. We performed AIMD simulations under the Born–Oppenheimer approximation to determine Na diffusivity in the NMPS system using VASP³⁸. Atom trajectories are calculated using Newtonian dynamics with Verlet integration in an NVT ensemble. A Nose–Hoover thermostat with a period of 40 timesteps (80 fs) was used for all simulations. Na-atom displacements are calculated with respect to the centre of mass of the framework (non-Na) atoms. Self-diffusivities from these simulations were calculated by fitting the Einstein relation of mean-squared displacements to time ($\langle \|\Delta \mathbf{x}\|^2 \rangle = 2dD_{\text{self}}t$), where d is the dimensionality, using tools implemented in the pymatgen software package³¹. Ionic conductivities taking into account correlations between Na-ions were calculated from the mean square displacement of the net Na-ion motion ($\langle \|\sum_{i=1}^n \Delta \mathbf{x}_i\|^2 \rangle = 2dD_{\sigma}nt$). Inserting D_{σ} into the Nernst–Einstein equation is equivalent to using the Green–Kubo expression for ionic conductivity when Na-ions are the only mobile charge carriers^{41,42}. The AIMD simulations were performed on a single unit cell of NMPS, with 50 ions (2 formula units). The volume and shape of the cells were obtained from the fully relaxed cells used for the energy calculations by enforcing tetragonal symmetry (equality of the a and b lattice parameters). The time step of the simulation was 2 fs. To reduce the computational cost of the calculation, forces were calculated using a single k -point. Temperatures were initialized at 300 K and scaled to the appropriate temperature over 1,000 time steps (2 ps), starting with the ground-state structure. Simulations between 600 and 900 K were 350,000 time steps (700 ps), and simulations above 900 K were 250,000 time steps (500 ps).

Calculation of the activation energy (E_a) and extrapolation of results to room temperature was performed with an Arrhenius fit to the diffusivity data. The Haven ratio, H_p , an indication of the cooperativity of ionic motion, is calculated from the ratio of D_{self} to the D_{σ} in each simulation.

Ionic probability density. Na-ion probability densities were calculated from the AIMD simulations. After enforcing $P4_2/mmc$ symmetry, Na-ion positions relative to the centre of mass of the framework (P, M, S) atoms were smoothed using a Gaussian kernel with s.d. of 0.2 Å, and the resulting density visualized using Vesta⁴³.

Fractional occupancies. Fractional occupancies were calculated using a k -means clustering algorithm⁴⁴, initialized with atomic positions from the structure of LGPS²⁶. At each clustering step, the shortest distance (taking into account periodic boundary conditions) to each mean was calculated, and a linear assignment algorithm⁴⁵ as implemented in pymatgen³¹ was used at each simulation time step to assign each Na-ion position to the nearest mean, ensuring that at most a single Na atom from each time step is assigned to any given mean. The resulting cluster sizes and centroids were used to define the occupancy and location of Na sites.

Synthesis. $\text{Na}_{10}\text{SnP}_2\text{S}_{12}$ was synthesized by mixing stoichiometric amounts of Na_2S (Kojundo Chemical Laboratory Co. Ltd, 99%), P_2S_5 (Sigma-Aldrich Co., 99%) and SnS_2 (Kojundo Chemical Laboratory Co. Ltd, 99.9%) with a planetary ballmill (380 r.p.m. for 17 h). The pelletized mixture was wrapped in gold foil and heated at 700 °C for 12 h in an evacuated quartz tube and slow-cooled down to room temperature for 99 h (approximately $-0.1^\circ \text{min}^{-1}$).

X-ray diffraction. The X-ray diffraction pattern is obtained with Cu–K α radiation (40 kV, 40 mA) from 10–90° 2 θ with 0.03° step intervals.

Conductivity measurement. Na-ion conductivity was measured with electrochemical impedance spectroscopy using an AUTOLAB PGSTAT30 (Metrohm Autolab, Utrecht) at 30, 40, 60 and 80 °C with a frequency ranging from 1 MHz to 100 mHz and an amplitude of 10 mV under normal pressure. An indium foil-blocking electrode was pressed onto both sides of the $\text{Na}_{10}\text{SnP}_2\text{S}_{12}$ pellet (11.5 mm diameter and 0.75 mm thickness). The conductivity values were obtained from the Cole–Cole plot of the data.

References

- Ellis, B. L. & Nazar, L. F. Sodium and sodium-ion energy storage batteries. *Curr. Opin. Solid State Mater. Sci.* **16**, 168–177 (2012).
- Kim, S.-W., Seo, D.-H., Ma, X., Ceder, G. & Kang, K. Electrode materials for rechargeable sodium-ion batteries: potential alternatives to current lithium-ion batteries. *Adv. Energy Mater.* **2**, 710–721 (2012).
- Pan, H., Hu, Y.-S. & Chen, L. Room-temperature stationary sodium-ion batteries for large-scale electric energy storage. *Energy Environ. Sci.* **6**, 2338 (2013).
- Ponrouch, A., Marchante, E., Courty, M., Tarascon, J.-M. & Palacin, M. R. In search of an optimized electrolyte for Na-ion batteries. *Energy Environ. Sci.* **5**, 8572 (2012).
- Komaba, S. *et al.* Electrochemical Na insertion and solid electrolyte interphase for hard-carbon electrodes and application to Na-ion batteries. *Adv. Funct. Mater.* **21**, 3859–3867 (2011).
- Palomares, V., Casas-Cabanas, M., Castillo-Martinez, E., Han, M. H. & Rojo, T. Update on Na-based battery materials. A growing research path. *Energy Environ. Sci.* **6**, 2312–2337 (2013).
- Hueso, K. B., Armand, M. & Rojo, T. High temperature sodium batteries: status, challenges and future trends. *Energy Environ. Sci.* **6**, 734–749 (2013).
- Khireddine, H., Fabry, P., Caneiro, A. & Bochu, B. Optimization of NASICON composition for Na⁺ recognition. *Sensors Actuators B Chem.* **40**, 223–230 (1997).
- Fergus, J. W. Ion transport in sodium ion conducting solid electrolytes. *Solid State Ionics* **227**, 102–112 (2012).
- Zhang, P., Matsui, M., Takeda, Y., Yamamoto, O. & Imanishi, N. Water-stable lithium ion conducting solid electrolyte of iron and aluminum doped NASICON-type $\text{LiTi}_2(\text{PO}_4)_3$. *Solid State Ionics* **263**, 27–32 (2014).
- Kamaya, N. *et al.* A lithium superionic conductor. *Nat. Mater.* **10**, 682–686 (2011).
- Seino, Y., Ota, T., Takada, K., Hayashi, A. & Tatsumisago, M. A sulphide lithium super ion conductor is superior to liquid ion conductors for use in rechargeable batteries. *Energy Environ. Sci.* **7**, 627–631 (2014).
- Hayashi, A., Noi, K., Sakuda, A. & Tatsumisago, M. Superionic glass-ceramic electrolytes for room-temperature rechargeable sodium batteries. *Nat. Commun.* **3**, 856 (2012).
- Hayashi, A., Noi, K., Tanibata, N., Nagao, M. & Tatsumisago, M. High sodium ion conductivity of glass-ceramic electrolytes with cubic Na_3PS_4 . *J. Power Sources* **258**, 420–423 (2014).
- Tanibata, N. *et al.* X-ray crystal structure analysis of sodium-ion conductivity in $94 \text{ Na}_3\text{PS}_4 \cdot 6 \text{ Na}_4\text{Si}_3\text{S}_{12}$ glass-ceramic electrolytes. *ChemElectroChem.* **1**, 1130–1132 (2014).
- Wang, Y., Xiao, R., Hu, Y.-S., Avdeev, M. & Chen, L. $\text{P}_2\text{-Na}_{0.6}[\text{Cr}_{0.6}\text{Ti}_{0.4}]\text{O}_2$ cation-disordered electrode for high-rate symmetric rechargeable sodium-ion batteries. *Nat. Commun.* **6**, 6954 (2015).
- Wang, Y. *et al.* A zero-strain layered metal oxide as the negative electrode for long-life sodium-ion batteries. *Nat. Commun.* **4**, 2635 (2013).
- Hautier, G., Fischer, C. C., Jain, A., Mueller, T. & Ceder, G. Finding nature’s missing ternary oxide compounds using machine learning and density functional theory. *Chem. Mater.* **22**, 3762–3767 (2010).
- Thangadurai, V., Narayanan, S. & Pinzaru, D. Garnet-type solid-state fast Li ion conductors for Li batteries: critical review. *Chem. Soc. Rev.* **43**, 4714–4727 (2014).
- Ong, S. P. *et al.* Phase stability, electrochemical stability and ionic conductivity of the $\text{Li}_{10\pm 1}\text{MP}_2\text{X}_{12}$ ($M = \text{Ge, Si, Sn, Al}$ or P , and $X = \text{O, S}$ or Se) family of superionic conductors. *Energy Environ. Sci.* **6**, 148–156 (2013).
- Whiteley, J. M., Woo, J. H., Hu, E., Nam, K.-W. & Lee, S.-H. Empowering the lithium metal battery through a silicon-based superionic conductor. *J. Electrochem. Soc.* **161**, A1812–A1817 (2014).
- Kuhn, A., Duppel, V. & Lotsch, B. V. Tetragonal $\text{Li}_{10}\text{GeP}_2\text{S}_{12}$ and Li_7GePS_8 – exploring the Li ion dynamics in LGPS Li electrolytes. *Energy Environ. Sci.* **6**, 3548–3552 (2013).
- Kuhn, A. *et al.* A new ultrafast superionic Li-conductor: ion dynamics in $\text{Li}_{11}\text{Si}_2\text{P}_{12}\text{S}_{12}$ and comparison with other tetragonal LGPS-type electrolytes. *Phys. Chem. Chem. Phys.* **16**, 14669–14674 (2014).
- Bron, P. *et al.* $\text{Li}_{10}\text{SnP}_2\text{S}_{12}$: an affordable lithium superionic conductor. *J. Am. Chem. Soc.* **135**, 15694–15697 (2013).
- Ong, S. P., Wang, L., Kang, B. & Ceder, G. Li-Fe-P-O₂ phase diagram from first principles calculations. *Chem. Mater.* **20**, 1798–1807 (2008).
- Kuhn, A., Koehler, J. & Lotsch, B. V. Single-crystal X-ray structure analysis of the superionic conductor $\text{Li}_{10}\text{GeP}_2\text{S}_{12}$. *Phys. Chem. Chem. Phys.* **15**, 11620–11622 (2013).
- Kandagal, V. S., Bharadwaj, M. D. & Waghmare, U. V. Theoretical prediction of a highly conducting solid electrolyte for sodium batteries: $\text{Na}_{10}\text{GeP}_2\text{S}_{12}$. *J. Mater. Chem. A* **3**, 12992–12999 (2015).
- Murch, G. The Haven ratio in fast ionic conductors. *Solid State Ionics* **7**, 177–198 (1982).
- Belsky, A., Hellenbrandt, M., Karen, V. L. & Luksch, P. New developments in the Inorganic Crystal Structure Database (ICSD): accessibility in support of materials research and design. *Acta Crystallogr. Sect. B Struct. Sci.* **58**, 364–369 (2002).
- Lepley, N. & Holzwarth, N. Computer modeling of crystalline electrolytes – lithium thiophosphates and phosphates. *ECs Trans.* **35**, 39–51 (2011).

31. Ong, S. P. *et al.* Python materials genomics (pymatgen): a robust, open-source python library for materials analysis. *Comput. Mater. Sci.* **68**, 314–319 (2013).
32. Sahu, G. *et al.* Air-stable, high-conduction solid electrolytes of arsenic-substituted Li_4SnS_4 . *Energy Environ. Sci.* **7**, 1053–1058 (2014).
33. Takada, K. *et al.* Interfacial modification for high-power solid-state lithium batteries. *Solid State Ionics* **179**, 1333–1337 (2008).
34. Hori, S. *et al.* Synthesis, structure, and ionic conductivity of solid solution, $\text{Li}_{10+\delta}\text{M}_{1+\delta}\text{P}_{2-\delta}\text{S}_{12}$ (M = Si, Sn). *Faraday Discuss* **176**, 83–94 (2014).
35. Kang, K. & Ceder, G. Factors that affect Li mobility in layered lithium transition metal oxides. *Phys. Rev. B* **74**, 094105 (2006).
36. Van der Ven, A. & Ceder, G. Lithium diffusion mechanisms in layered intercalation compounds. *J. Power Sources* **97–98**, 529–531 (2001).
37. Jansen, M. & Henseler, U. Synthesis, structure determination, and ionic conductivity of sodium tetrathiosphosphate. *J. Solid State Chem.* **99**, 110–119 (1992).
38. Kresse, G. & Furthmüller, J. Efficient iterative schemes for ab initio total-energy calculations using a plane-wave basis set. *Phys. Rev. B* **54**, 11169–11186 (1996).
39. Blöchl, P. E. Projector augmented-wave method. *Phys. Rev. B* **50**, 17953–17979 (1994).
40. Perdew, J. P., Burke, K. & Ernzerhof, M. Generalized gradient approximation made simple. *Phys. Rev. Lett.* **77**, 3865–3868 (1996).
41. Helfand, E. Transport coefficients from dissipation in a canonical ensemble. *Phys. Rev.* **119**, 1–9 (1960).
42. Uebing, C. & Gomer, R. Determination of surface-diffusion coefficients by Monte-Carlo methods - comparison of fluctuation and Kubo-Green methods. *J. Chem. Phys.* **100**, 7759–7766 (1994).
43. Momma, K. & Izumi, F. VESTA: a three-dimensional visualization system for electronic and structural analysis. *J. Appl. Crystallogr.* **41**, 653–658 (2008).
44. Lloyd, S. Least squares quantization in PCM. *Inf. Theory, IEEE Trans.* **28**, 129–137 (1982).
45. Jonker, R. & Volgenant, A. A shortest augmenting path algorithm for dense and sparse linear assignment problems. *Computing* **340**, 325–340 (1987).

Acknowledgements

We thank Dr Rahul Malik for comments on an early version of the manuscript. This work was supported by Samsung Advanced Institute of Technology and computational resources were provided by the Extreme Science and Engineering Discovery Environment (XSEDE), which is supported by National Science Foundation grant number ACI-1053575.

Author contributions

W.D.R., S.P.O. and G.C. designed the computational study. Synthesis and experimental analysis was performed by T.T., I.U. and N.S. W.D.R. performed the computational experiments and prepared the manuscript. W.D.R., L.J.M., J.K. and Y.W. analysed and interpreted the data. All authors discussed results and commented on the manuscript.

Additional information

Supplementary Information accompanies this paper at <http://www.nature.com/naturecommunications>

Competing financial interests: The authors declare no competing financial interests.

Reprints and permission information is available online at <http://npg.nature.com/reprintsandpermissions/>

How to cite this article: Richards, W. D. *et al.* Design and synthesis of the superionic conductor $\text{Na}_{10}\text{SnP}_2\text{S}_{12}$. *Nat. Commun.* **7**:11009 doi: 10.1038/ncomms11009 (2016).



This work is licensed under a Creative Commons Attribution 4.0 International License. The images or other third party material in this article are included in the article's Creative Commons license, unless indicated otherwise in the credit line; if the material is not included under the Creative Commons license, users will need to obtain permission from the license holder to reproduce the material. To view a copy of this license, visit <http://creativecommons.org/licenses/by/4.0/>